## Ultrasensitive nonlinear vibrational spectroscopy of complex molecular systems

Selig, O.

**Publication date**
2017
**Document Version**
Other version
**License**
Other

# CHAPTER 3

# EXPERIMENT

This chapter will present the pump-probe and 2DIR setup used for the experiments in this thesis. In addition, some aspects of the data acquisition and data processing will be discussed in detail.

## 3.1 LIGHT GENERATION

In our experiments the wavelengths of the pump and probe pulses can be tuned independently in the range 1.1–10 μm. In order to generate these pulses we start with a regeneratively amplified femtosecond laser system, after which a number of nonlinear conversion steps are used to reach the midinfrared wavelength region.

### 3.1.1 LASER SYSTEM

The starting point of the laser system is a Ti:Sapphire oscillator (Coherent, Mantis-5) which generates pulses at 811 nm (bandwidth > 80 nm) at a repetition rate of 80 MHz

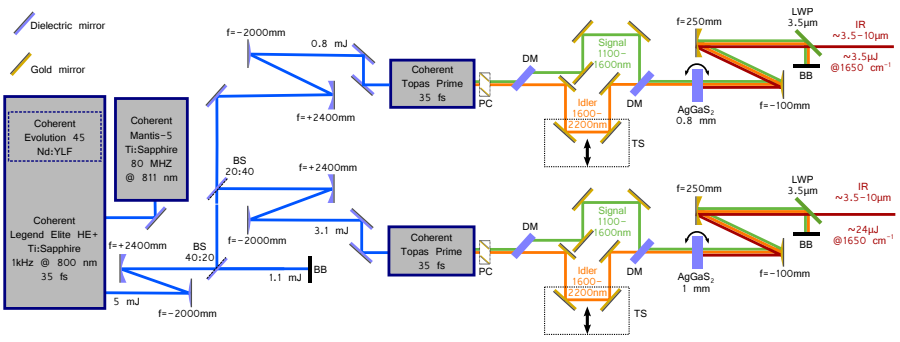


FIGURE 3.1. Generation of mid-infrared femtosecond pulses. BS: beam splitter. DM: dichroic mirror. $AgGaS_2$: silver-gallium-disulfide crystal with indicated thickness. LWP: longwave pass filter. BB: beam block. TS: translation stage. PC: periscope.

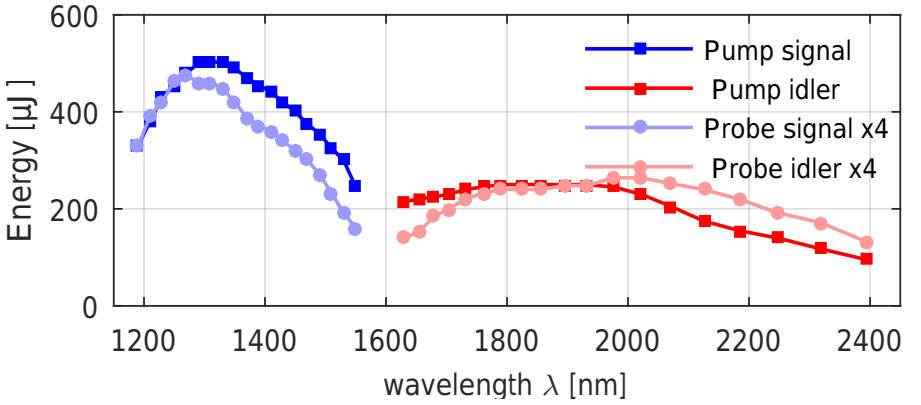


FIGURE 3.2. Signal and idler energies of the pump and probe OPAs as a function of wavelength.

with an output power of ∼ 580 mW. The output from the oscillator is used to seed a Ti:sapphire regenerative amplifier (Coherent, Legend Elite-USP-1K-HE+). The crystal in the amplifier is pumped by an internal ND:YLF laser (Coherent, Evolution 45, 1 kHz, 28 mJ) with a wavelength of 527 nm. After entering the amplifier, the seed pulse is stretched by a pair of gratings to reduce its peak intensity. 1 out of 80 000 seed pulses is coupled into the cavity of the amplifier via a Pockels cell. After 10 round trips through the pumped Ti:Sapphire crystal the amplified pulse is extracted using a second Pockels cell, and lastly, recompressed using a second set of gratings. The amplifier yields p-polarized 35 fs pulses (∼5 mJ) at 800 nm with a repetition rate of 1 kHz.
In order to reduce the power density on the following dielectric optics the diameter of the 800 nm beam is expanded by a factor 1.2 using a telescope. Next, two 80:20 beam splitters are used to split the 800 nm beam into three beams: a ∼0.8 mJ beam for the probe path, a ∼3.2 mJ beam for the pump path and an additional ∼1.1 mJ beam. The diameter of the beams for the pump and probe path are decreased using telescopes (factor: 1.2), and the beams are guided into two commercial optical parametric amplifiers (OPA; Coherent, TOPAS Prime).

### 3.1.2 OPTICAL PARAMETRIC AMPLIFIERS

The two OPAs constitute the first light conversion steps, and they each generate two output beams—signal (1.1-1.6
textmu m, s-polarized) and idler (1.6-2.2 μm, p-polarized)—with a power conversion efficiency of ∼ 30%[a]. The OPAs operate in two stages. In the first stage, two beams, each containing a small fraction (∼5%) of 800 nm light are split off. The first beam is focused into a sapphire crystal to generate a white-light continuum (WLC) and is consecutively frequency mixed with the delayed second beam inside a $\beta$-barium-borate (BBO) crystal. By choosing the delay between the strongly chirped WLC and

[a] ((signal+idler)/input)

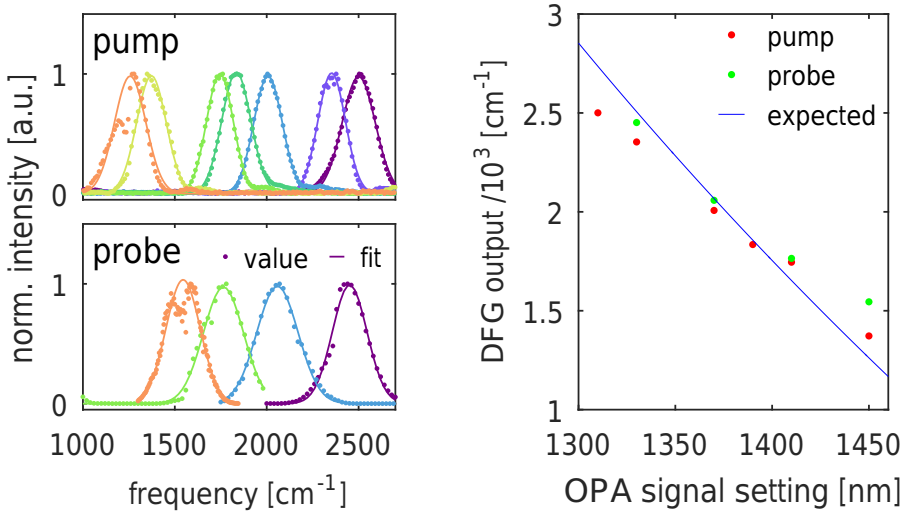


FIGURE 3.3. left: Example spectra of the infrared light generated by frequency mixing signal and idler beams in silver-gallium-disulfide for the pump and probe path. right: Center frequency of the infrared light generated by the difference frequency mixing process as a function of the selected OPA signal wavelength (red and green dots) compared to the expected values (blue line).

the 800 nm beam and the angle of the BBO-crystal, a specific frequency component can be selected and amplified. The amplified signal[b] beam is spatially isolated and used as a seed beam for the second stage. In the second stage the seed (signal) is combined with the remaining 800 nm light (∼90%) in a second BBO-crystal to generate the actual two output beams of the OPA.
The wavelength of the two output beams is set by four parameters: the angle of the BBO crystal in the first and second stage, the delay between the white-light and the 800 nm beam in the first stage, and the delay between the first and the second stage. All parameters can be set by computer controlled translation and rotation motors. After initial calibration of all motors, the wavelengths of signal and idler can directly be selected via a software interface. Figure 3.2 shows the measured energies for signal and idler as a function of frequency for both OPAs.

### 3.1.3 DIFFERENCE-FREQUENCY GENERATION

To arrive at wavelengths in the mid-infrared (3-10 μm ) an additional nonlinear light conversion step is necessary. The conversion efficiency strongly depends on the quality of the temporal and spatial overlap of the signal and idler beams. Since both beams exit the OPA almost collinearly with a small time separation, they are initially separated onto two independent optical paths by a dichroic mirror, guided over a

[b]The three beams involved in difference frequency generation referred to as pump, signal, idler with the frequency ordering $\omega_{pump} > \omega_{signal} > \omega_{idler}$

retroreflector, and subsequently recombined onto a common path using a second dichroic mirror. The retroreflector in the idler path is mounted on a mechanical translation stage which allows to adjust the time delay between both paths. Lastly, the beams are difference-frequency mixed using a silver-gallium-disulfide (AGS, $AgGaS_2$) crystal. The generated p-polarized infrared beam is isolated by a germanium-based long-wave-pass filter (LWP, $\lambda > 3.4$ μm ), and the signal and idler pulses are discarded onto a beam block (BB). Lastly, telescopes are used in the pump and probe paths to expand the beam size to ⌀3.8 mm and ⌀5.0 mm, respectively. Figure 3.3 shows example spectra of the generated infrared light and compares their center frequencies with expected values for the selected signal wavelengths.

## 3.2 PUMP-PROBE EXPERIMENT

Having described the generation of the infrared light, we will next discuss the implementation of the pump-probe experiment in this section. To this end, we will first summarize the working principle of the experiment, then present the experimental realization and, lastly, have an extended look at the detection of the infrared light with an MCT-detector.

### 3.2.1 OPERATING PRINCIPLE

During a pump-probe (pp) experiment we use the probe pulse to measure the pump-induced absorption change $\Delta\alpha$ of the sample. To this end, the transmission spectrum of the probe pulse is normalized to the reference spectrum ($T = \frac{I_{probe}(\nu)}{I_{ref}(\nu)}$) and measured in the presence and absence of a pump pulse. The normalization to the reference spectrum $I_{ref}$ serves to compensate for fluctuations in the laser spectrum. This normalization results in a significant increase in the signal-to-noise ratio.[67] The pump-induced absorption change is given by:

$$\Delta\alpha(\nu) = -\log_{10}\left(\frac{T_{pump}(\nu)}{T_0(\nu)}\right) = -\log_{10}\left(\frac{I_{probe,pump}(\nu)\cdot I_{ref,0}(\nu)}{I_{probe,0}(\nu)\cdot I_{ref,pump}(\nu)}\right) \tag{3.1}$$

where the subscripts $0$ and $pump$ refer to a measurement in the absence or presence of the pump pulse. To measure the dynamic processes inside the sample, e.g. to monitor the vibrational relaxation, the time $t_{pp}$ between the pump and probe pulse is varied. Performing polarization-resolved experiments allows us to disentangle the measured absorption change into an isotropic contribution ($\Delta\alpha_{iso}$) which reflects the decay of the excited state population, and an anisotropic contribution ($R(t)$) which provides information about the orientational motion of the transition dipole moment that is probed (see Section 2.4.4).

### 3.2.2 SETUP: OPTICS

The description of the pump-probe experiment is presented in three parts: pump, probe and detection path. Figure 3.4 shows an overview of all three parts.

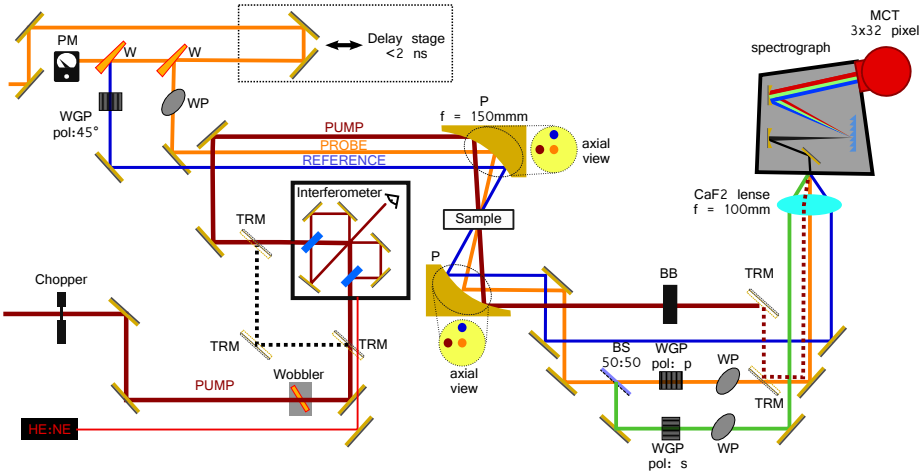


FIGURE 3.4. Pump-probe and 2DIR setup. PM: power meter. WGP: wiregrid polarizer. WP: waveplate. P: parabolic mirrors. BB: beam block. TRM: temporary routing mirror. W: ZnSe wedge. BS: beam splitter.

### PUMP PATH

The pump beam first passes through a chopper (Thorlabs, MC2000). The chopper is synchronized to the laser, operates at 500 Hz, and blocks every other shot during a pump-probe experiment. Next, the beam is guided through a wobbling ZnSe-window (wobbler, AMOLF). The wobbler is used to minimize artifacts in the nonlinear signal which originate from pump-light (scattering) reaching the detector (see Section 3.4). For the 2DIR experiments, the beam is coupled into a Mach-Zehnder interferometer which allows for modulation of the pump spectrum (Section 3.3). Conveniently the interferometer can also be used to monitor the pump spectrum. For the pump-probe experiments the interferometer is bypassed by inserting temporary routing mirrors (TRM) into the beam path.

### PROBE PATH

The probe beam is first guided over a retroreflector mounted on top of a computer-controlled translation stage (PI, M-414.3pd) with a travel range of 30 cm, which allows a precise control of the time delay between the pump and probe pulse from ∼10 fs up to 2 ns. Next, two ZnSe-wedges (45°, $R \approx 10\%$) are used to split off two reflections from the beam, so that the actual probe (∼200 nJ) and reference (∼200 nJ) are generated. The polarization of the probe beam is set to 45° relative to the pump beam polarization (and the normal of the table), which allows for simultaneous detection of $\Delta\alpha_{\parallel}$ and $\Delta\alpha_{\perp}$ (see below).

### DETECTION PATH

Next, all three beams—pump, probe and reference—are focused into the sample using an off-axis gold parabolic mirror (90°, f = 15 cm). Pump and probe overlap spatially while the reference beam is displaced by a small distance. Behind the

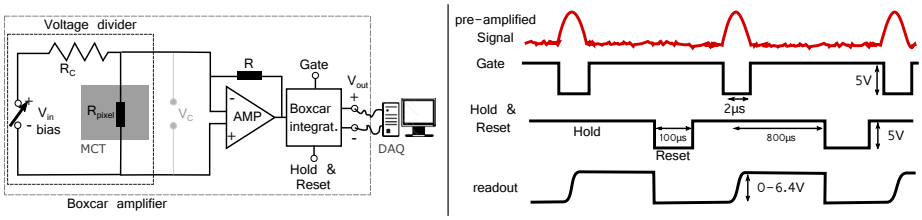


FIGURE 3.5. left: simplified detection circuit. An adjustable input voltage $V_{in}$ is divided over a fix resistor $R_c$ and the photoresistor $R_{pixel}$. The change in the extracted voltage $V_c$ upon illumination, is amplified by an operation amplifier (AMP) and integrated using a boxcar integrator to yield the output $V_{out}$. right: Boxcar integration timing. The integration window of the pre-amplified signal is defined by a gate pulse (TTL, 2 µs). The integrated voltage is held for readout until an additional pulse (TTL, 100 µs) resets the integrators ∼ 100 µs before the next pulse arrives.

sample, the three beams are recollimated using an identical parabolic mirror. After the second parabolic mirror, the pump beam is discarded onto a beam block (during the experiments). Alternatively, it can be guided to the detector (for alignment purposes) using a flip mirror along the probe path.
Behind the sample, the probe beam is split into two independent paths, by a nonpolarizing 50:50 beamsplitter. In each path one polarization component is selected, either parallel (p) or perpendicular (s) to the pump polarization, using wire-grid polarizers. Both probe beams and the reference beam are coupled into a spectrograph (Oriel, MS260i). The beams are detected by a liquid-nitrogen-cooled mercury-cadmium-telluride detector (MCT, Infrared associates, 3x32 pixel).

### 3.2.3 SETUP: ELECTRONICS

#### INFRARED DETECTION

During the experiment three spectra (reference, probe$_{||}$, probe$_{\perp}$) are recorded simultaneously. In order to read, save and process the infrared signal the intensity of the incident light needs to be converted into a voltage. This is achieved by using three hardware components for each spectrum: one line of the MCT detector (32 pixel), one boxcar integrator (AMOLF), and one data acquisition card (DAQ-card, National Instruments, PXI-6225).
Figure 3.5 shows a schematic representation of the detection circuit. Every MCT pixel is a photoresistor ($R_{MCT} \sim 100\Omega$) which changes its resistance upon illumination ($\Delta R \sim 1/10\Omega$). The resistance change is converted into a voltage change by a voltage-dividing circuit consisting of an adjustable power source ($V_{in}$, bias), a reference resistor $R_c = 100\Omega$ and the MCT pixel. The voltage change is first amplified by an operational amplifier and then integrated using a gated boxcar integrator. The response of the amplified voltage divider to an infrared pulse has a temporal width of ∼ 1.5 µs. By choosing the integration window slightly broader (2 µs), one can minimize the noise originating from jitter in the laser timing (Figure 3.6a). Lastly, the integrated signal is digitized by the DAQ-cards (16 bits). The

maximum readout voltage of the boxcar integrators is around 6.4 V and it is fixed by the circuit design. Therefore, the dynamic range of the voltage measurement is determined by the resolution of the DAQ-card and the maximum voltage. One can, however, adjust the gain between incident light and generated voltage by choosing the width and timing of the gate pulse, and/or by choosing the bias current. It is advantageous to maximize the dynamic range of the optical measurement[cd] to increase the signal-to-noise ratio (see below) and prevent artifacts originating from the voltage discretization by the DAQ-cards.

Special care must be taken when increasing the bias current since, as a side effect, it can also increase the noise of the detection circuit. Figure 3.6 shows the measured dark noise of the complete detection circuit as a function of the applied bias current. This dark noise $\sigma_{det}$ is completely random, and therefore it is the ultimate factor that limits the maximally achievable signal-to-noise ratio. Assuming perfect alignment, i.e. the fluctuations of the laser spectrum are completely compensated for by reference normalization, one can propagate the error of the voltage measurement ($V_{ref}$, $V_{probe}$) to estimate the relative noise in the transmission measurement $\frac{\sigma_T}{T}$ and in the absorption change $\frac{\sigma_{\Delta\alpha}}{\Delta\alpha}$ to:

$$\frac{\sigma_T}{T} = \sqrt{\left(\frac{\sigma_{det}}{V_{probe}}\right)^2 + \left(\frac{\sigma_{det}}{V_{ref}}\right)^2} \approx \sqrt{2}\frac{\sigma_{det}}{V_{probe}} \approx 0.07\% \tag{3.2}$$

$$\frac{\sigma_{\Delta\alpha}}{\Delta\alpha} \approx 2\frac{\sigma_{det}}{V_{probe}} \approx 0.1\% \tag{3.3}$$

where 1.5 mV and 3 V was used for $\sigma_{det}$ and $V_{probe}$ respectively. The difference of $\sqrt{2}$ between the two equations originates form the fact that $\Delta\alpha$ is computed as the ratio of two transmission measurements.

In summary, one should aim at having the highest possible readout voltage while simultaneously keeping the bias current as low as possible.

### DETECTOR CALIBRATION

Figure 3.6d shows that the detected voltage does not scale perfectly linearly with the light intensity. This nonlinearity can have a severe impact on the measured transient spectrum, especially for samples for which absorption varies strongly over the spectrum. Therefore, it is necessary to first linearize the detector signal before using it to compute the transient spectrum. To this end, we use a calibration function $C(V, pix)$ to convert the measured voltage $V$ into a quantity which depends linearly on the light intensity. In order to construct the calibration function, we first record the response of every pixel as a function of the light intensity $V(I, pix)$. This is achieved with the help of two polarizers in the probe path which act as a variable attenuator for the three detected beams. The relative light intensity $I$ is determined (up to an arbitrary scaling factor) with the help of a calibrated pyroelectric detector

[c] largest intensity difference/ smallest intensity difference

[d] In a typical pump-probe measurement the absorption of the band of interest is adjusted to $\alpha \approx 1$ OD and the absorption change is detected to better than $\Delta\alpha \approx 0.5$ mOD

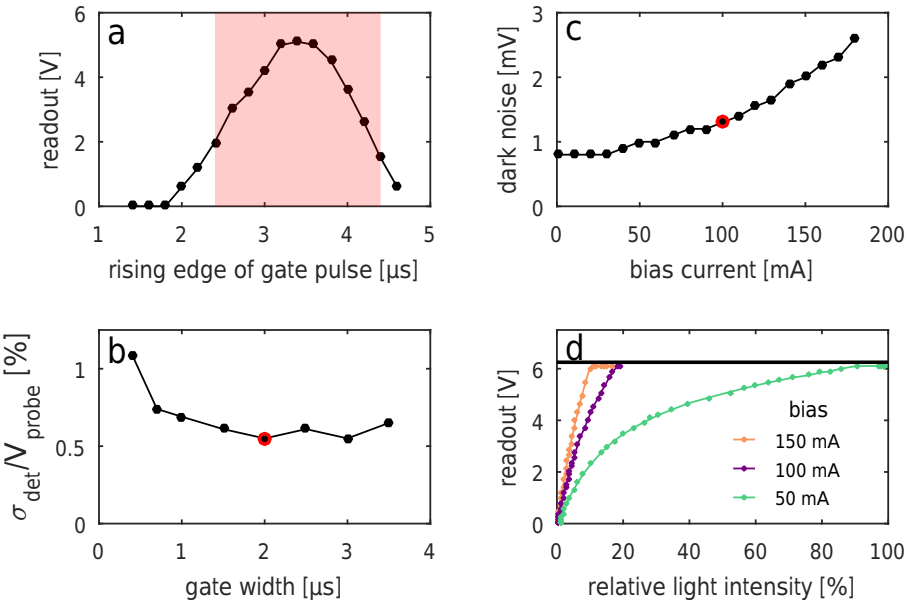


FIGURE 3.6. a: Pre-amplified voltage obtained by scanning the gate pulse (bias 100 mA per 16 pixel). Red shaded area indicates the gate pulse. b: Relative noise for a given readout Voltage (3 V) and bias current (100 mA per 16 pixel) as a function of gate width. c: Dark noise for one pixel (100 mA per 16 pixel, gate 2 µs). d: Voltage as a function of illumination for different bias currents (gate 2 µs). Red marks indicate the values used for the experiments in this thesis.

placed behind one of the ZnSe wedges in the setup (Figure 3.4). Typically, the voltage of a pixel $V(I, pix)$ saturates asymptotically as a function of the light intensity (see Figure 3.6d), and this functional dependence was found to be very well described by:

$$V(I, pix) = \frac{a_2 I}{a_1 + I}. \tag{3.4}$$

By inverting $V(I, pix)$, we find the correction function $C(V, pix)$ to be given by:

$$C(V, pix) = \frac{V a_1(pix)}{a_2(pix) - V} \tag{3.5}$$

where $a_2(pix)$ is the saturation voltage (at $I = \infty$) and $a_1(pix)$ is an arbitrary scaling factor which reflects the sensitivity of the pixel. By fitting $V$ as a function of $I$ we find $a_1(pix)$ and $a_2(pix)$ and hence the correction function $C(V, pix)$. This allows us to convert the recorded voltage of every pixel into a signal that is proportional to the incident light intensity.

At this point, the detector is calibrated, so that it is possible to correctly measure pump-probe and 2DIR signals. A final issue that needs to be addressed is the fact that the sensitivities of the individual pixels vary greatly (i.e. $a_2/a_1$ is different for

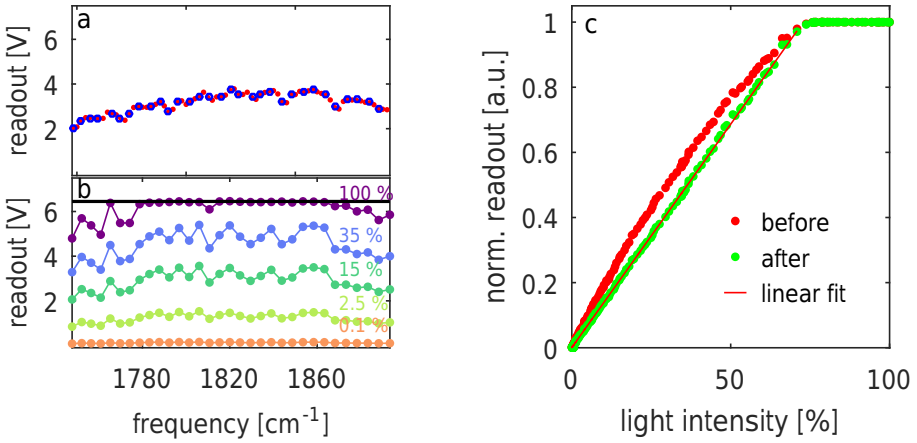


FIGURE 3.7. a: Spectrum obtained by scanning the spectrometer grating and recording the voltage for one pixel. Blue circles indicate values which were selected to match the pixels in the intensity series. b: Light intensity series. Shown is the voltage spectrum at a given relative illumination for the 32 pixels of the probe array. c: Normalized voltage as a function of light intensity for one pixel of the probe array before and after calibration. The plateau at a relative light intensity above 80 % originates from (electronic) saturation of the detector.

every pixel). Fortunately, this problem can be solved straightforwardly by scaling the parameters $a_1(pix)$ with respect to each other. The scaling factors are found by using the array detector to measure the spectrum of a light pulse and comparing this to a measurement in which a single pixel is used while the grating is scanned. While this variation does not affect the transient signal (which is independent of the absolute pixel sensitivity), it poses problems when the array is used to measure the intensity spectrum of a light pulse. Figure 3.7 shows the response for one pixel before and after calibration.

## 3.3 2DIR EXPERIMENT

The first 2DIR measurements were performed in the pump-probe geometry with an etalon (Fabry-Perot) placed in the pump beam to produce a narrow-band pump pulse ($\sim$15 cm$^{-1}$).[77] The two dimensional spectrum was generated by scanning the center frequency of the pump pulse and recording a transient spectrum for a range of pump frequencies. Although this frequency-domain approach is straightforward in its implementation and still widely used today, it comes at the cost of limited time resolution since it generates pump pulses with a duration of 0.5 — 1.0 ps.
All 2DIR spectra in this thesis are measured in the time-domain by employing a Mach-Zehnder (MZ) interferometer (Figure 3.13). As in the Fabry-Perot approach, the experiment is performed in the pump-probe geometry, but now the etalon is replaced by an MZ interferometer (see Figure 3.4). The advantages of the Mach-Zehnder method are that ultrashort pulses (<0.5 ps) can be used to obtain a high frequency resolution, and that the absorption change is measured simultaneously at all pump frequencies. In addition, one has the possibility to perform experiments where the two pump pulses have different polarizations. This offers certain advantages by providing additional experimental freedom and is obviously not possible with the Fabry-Perot approach.[78]
In the following section we will first discuss some general principles common to all Fourier transform spectroscopic techniques, such as the influence of the window function and the accessible resolution. In the second part we will describe the acquisition and processing of time-domain 2DIR spectra.

### 3.3.1 GENERAL PRINCIPLES OF FOURIER TRANSFORM SPECTROSCOPY

There are three main advantages of Fourier transform spectrometers (FTS) compared to dispersive spectrometers:[79]

- **Fellgett advantage** (multiplexing): In a dispersive spectrometer all wavelengths are collected consecutively, whereas in an FTS all wavelengths are collected simultaneously, resulting in a faster acquisition of the complete spectrum.

- **Jacquinot advantage** (throughput): The power throughput of a dispersive spectrometer is lower compared to the FTS due to the need of entrance and exit slits. This results in higher signal-to-noise when measuring with an FTS with the same experimental parameters (such as acquisition time, spectral range, resolution).

- **Connes advantage** (frequency calibration): The frequency axis of a dispersive spectrometer is defined by calibration (e.g with samples with well known absorption lines). In a FTS the frequency axis is derived from a (very well known) reference laser (mostly HeNe), resulting in much better long-term stability.

#### INTERFEROMETRY

Figure 3.8 shows a Michelson interferometer, where the light propagates from the

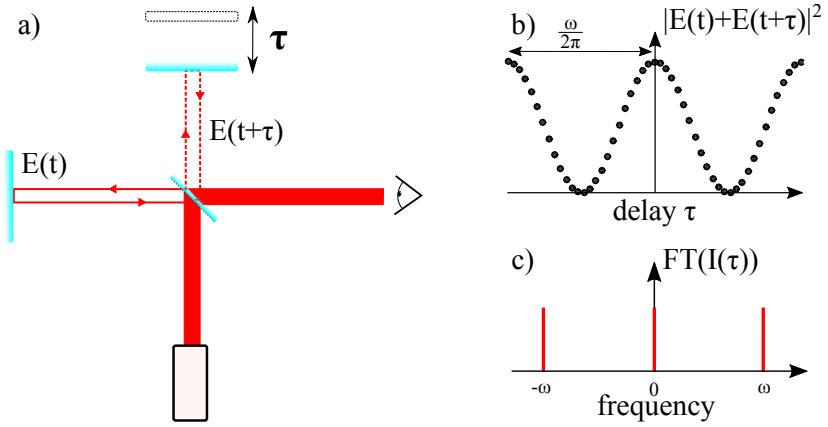


FIGURE 3.8. a) Michelson Interferometer: Light is split and recombined using a beamsplitter and measured by a slow photodetector. The end mirror of one arm can be moved to introduce a time delay $\tau$. b) Measured intensity signal $I(\tau)$ as a function of displacement $\tau$ of a monochromatic light source. c) Fourier transform of $I(\tau)$

source to a 50:50 beamsplitter, is split up into two arms, reflected by end-mirrors in each arm, recombined by the same beamsplitter and lastly observed by a detector. One of the end-mirrors can be moved to introduce a path length difference, between the two arms:

$$\Delta x = 0.5\tau c. \tag{3.6}$$

Here $\tau$ is the time difference between the two paths and $c$ the speed of light. For now, we assume that the electric field emitted by the light source is a monochromatic plane wave of the form:

$$E(t) = E_0 \exp^{i(k_0 x - \omega_0 t)} + c.c. \tag{3.7}$$

with real amplitude $E_0$. The total electric field $E_{tot}$ at the position of the detector ($x = 0$) is given by the sum of the fields from the static $E(t)$ and the dynamic arm $E(t+\tau)$:

$$E_{tot}(t,\tau) = E(t) + E(t+\tau) = E(t)\left(1 + e^{-i\omega_0\tau}\right) + c.c. \tag{3.8}$$

Since most detectors (e.g. MCT, eye) are slow relative to the fast oscillating electric field, only the time averaged intensity over a time period $T$ which is much longer than one light cycle can be measured:[80]

$$I(\tau) = 0.5 c\epsilon_0 \left\langle E_{tot}^2 \right\rangle_T = \frac{c\epsilon_0}{2T} \int_{t'}^{t'+T} dt' \, \mathcal{R}e\left(E_{tot}(t',\tau) E(t',\tau)^*_{tot}\right) \tag{3.9}$$

$$= c\epsilon_0 E_0^2 (1 + \cos(\omega_0 \tau)) \tag{3.10}$$

where the asterisk denotes the complex conjugate. Fourier transformation[e] of Equation 3.10 yields:

$$I(\omega) = \mathscr{F}(I(\tau)) \tag{3.11}$$

$$= c\epsilon_0 E_0^2 \left( \int_{-\infty}^{\infty} e^{-i\omega\tau} d\tau + \int_{-\infty}^{\infty} \cos(\omega_0\tau) e^{-i\omega\tau} d\tau \right) \tag{3.12}$$

$$= 0.5 c\epsilon_0 E_0^2 (2\delta(0) + \delta(\omega_0 - \omega) + \delta(\omega_0 + \omega)) \tag{3.13}$$

The first term originates from the constant offset (dc), the second and third term carry the frequency of the modulation.
If the electric field consist of a linear combination of two or more frequencies, then the interferogram $I(\tau)$ is given by a linear combination of frequency dependent cos-terms, since all other cross-terms vanish in Eq. 3.13. Therefore, it is straightforward to extend the discussion above to polychromatic light:

$$E(t) = \int_{-\infty}^{+\infty} E(\omega) e^{-i\omega t} d\omega + c.c. \tag{3.14}$$

$$I(\tau) = c\epsilon_0 \int_{-\infty}^{\infty} E^2(\omega)(1 + \cos(\omega\tau))\, d\omega \tag{3.15}$$

$$I(\omega) = \int_{-\infty}^{\infty} I(\tau) e^{-i\omega\tau} d\tau. \tag{3.16}$$

Here $E(\omega)$ is the spectral distribution. In reality, $\tau$ can neither be measured continuously nor varied until infinity. The implications of these limitations will be discussed in the following sections.

### RESOLUTION

In any spectroscopic experiment, it is important to be aware of the resolution, i.e. the minimum frequency spacing that two spectral lines need to have in order to be distinguishable as separate lines. To estimate the resolution in FTS, we first recall the *convolution theorem*:[81]

$$\mathscr{F}(f(t) \cdot g(t)) = \mathscr{F}(f(t)) * \mathscr{F}(g(t)) \tag{3.17}$$

which states that the Fourier transform of the product of two functions equals the convolution of their Fourier transforms. It is important to realize that there is at least one product in any interferometric experiment. Even in the simple case of monochromatic light, we are limited by a finite scan length $L$ which can be described as an infinitely long interferogram multiplied by a finite rectangular window (boxcar)

[e] Throughout the text we will use $\mathscr{F}(f(t)) = \int_{-\infty}^{\infty} f(t) e^{-i\omega t}$ for the Fourier transform and $\mathscr{F}(f(\omega)) = \frac{1}{2\pi} \int_{-\infty}^{\infty} f(\omega) e^{i\omega t}$ for the inverse Fourier transform.

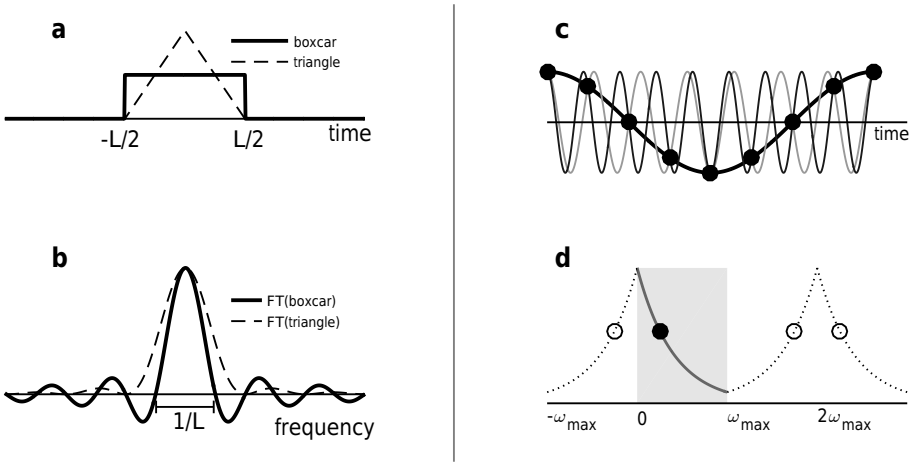


FIGURE 3.9. Apodization and Backfolding a) Two common window functions: boxcar (finite interferogram) and triangular function. b) The respective Fourier transforms: sinc and sinc$^2$. c) A sampled (dots) sine wave signal $S$ (bold line), and sine waves with higher frequency perfectly matching the same sampling points. d) Unique frequency window (gray) $[0;\omega_{max}]$ for a given sampling rate. Filled circle corresponds to the frequency of the signal $S$ (the bold line in c)) and the empty circles represent sine waves with high frequency matching the same sampling points.

function:

$$D(t) = 1 \quad \text{for} \quad t < |\frac{L}{2}| \tag{3.18}$$

$$= 0 \quad \text{for} \quad t > |\frac{L}{2}| \tag{3.19}$$

with the corresponding Fourier transform:[82]

$$\tilde{D}(\omega) = L\frac{\sin\left(\frac{\omega L}{2}\right)}{\frac{\omega L}{2}} \equiv L\,\mathrm{sinc}\left(\frac{\omega L}{2}\right) \tag{3.20}$$

Due to the convolution, the resulting spectrum will have a finite linewidth in the frequency domain even if we had a perfectly monochromatic source ($\delta$-peaks). From Equation 3.20 one can see that in this case *the width of the spectral line is solely determined by the scanned distance L*.

One common criterion to define resolution is: two peaks are resolved if the two maxima are separated by a dip with an amplitude of 20% of the maximum amplitude. In the case of a square window function and perfectly sharp frequencies (monochromatic), the frequency resolution $\omega_{res}$ is given by:[79]

$$\omega_{res} \approx 0.75\frac{4\pi c}{L} \tag{3.21}$$

Of course, in a real experiment we do not measure infinitely sharp spectral lines. Therefore Equation 3.21 provides an upper limit for the best possible resolution at a given scan distance. It is important, however, to realize that the used window function (so far boxcar) influences the observed lineshapes via the convolution theorem (Eqn. 3.17).

In general, one can multiply the time-domain signal with any arbitrary function. This process is called apodization and is essentially equivalent to choosing the lineshape function (LSF) in the frequency domain. Figure 3.9 shows, as an example, the comparison between the square and triangular window function in the time and frequency domain. Ideally we would like to choose an apodization function which is infinitely narrow in the frequency domain, and therefore does not result in line broadening; and which does not have any sidelobes which could potentially be mistaken for real spectral features (peaks)[f]. However, there are certain limitations to the choice. The LSF can be characterized by two parameters: the full width at half maximum (FWHM) and the height of the largest secondary maximum. Norton and Beer found an empirical limit for how small the FWHM can get for a given side lobe magnitude[g].[83] This means, it is up to the experimenter to choose between LSFs which conserve narrow lines, or have low side lobes, or are the ideal compromise of the two for a given experiment.

### SAMPLING

In the previous section it was shown that the choice of the scan length and window function have a severe impact on the observed spectral lineshapes. However, it is not yet clear how finely the time-domain data need to be sampled between the start and end position. Since the application of a Fourier transform implicitly assumes that the given data set is periodic, this question can be reformulated to: how many data points per period are needed to uniquely define a sine wave. Unfortunately, this question cannot be answered without additional information, since for every sampling frequency $1/\Delta\tau$ of a sine wave, there exist an infinite amount of sine waves with higher frequencies which exactly fit the same sampling points (see Figure 3.9c, d).

Hence, we impose that the measured signal is bandwidth-limited, i.e. there exists a maximum frequency component $\omega_{max}$ in the signal, and all higher frequency components are zero. The sampling of a continuous time domain signal $f(\tau)$ at every time step $\Delta\tau$ can be described, by the multiplication of $f(\tau)$ with a Dirac-comb

[f] The magnitude of the first minimum of the sinc function is about 22% of the magnitude of its absolute maximum.

[g] The empirical limit determined by Norton and Beer is

$$\log_{10}\frac{h}{h_0} \approx 1.939 - 1.401\left(\frac{W}{W_0}\right) - 0.597\left(\frac{W}{W_0}\right)^2 \tag{3.22}$$

where $h/h_0$ is the size of the first sidelobe of the apodization function relative to the sinc-function, and $(W/W_0)$ the ratio of the widths.[83]

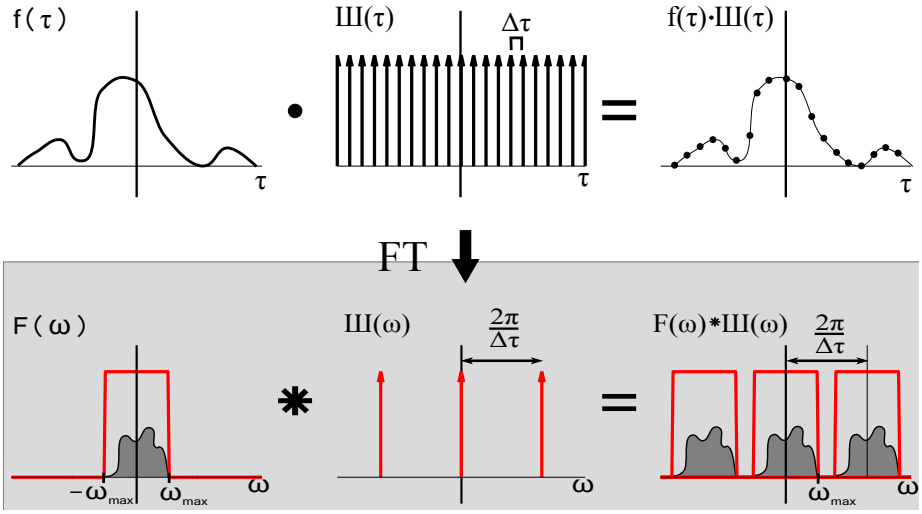


FIGURE 3.10. Fourier transform of a bandwidth limited, sampled, time domain signal. A time-domain signal which is sampled at every $\Delta\tau$ is given by the product of a continuous function $f(\tau)$ (here: sinc-function) and a Dirac-comb $\text{Ш}(\tau)$ (top). The product in time domain results in a convolution in frequency domain, leading to replication of the spectrum at a period of $2\pi\Delta\tau$.

(Fig. 3.10):

$$f^*(\tau) = f(\tau)\text{Ш}_{\Delta\tau}(\tau) \tag{3.23}$$

$$\text{Ш}_{\Delta\tau}(\tau) = \sum_{n=-\infty}^{+\infty} \delta(\tau - n\Delta\tau) \tag{3.24}$$

The Dirac-comb $\text{Ш}_{\Delta\tau}(\tau)$ is defined as the sum of an infinite number of equally spaced Dirac-deltas $\delta$, and its subscript indicates the sampling step. Since the Dirac-comb is a periodic function it can also be written as a Fourier series:

$$\text{Ш}_{\Delta\tau}(\tau) = \frac{1}{\Delta\tau} \sum_{n=-\infty}^{+\infty} e^{in\omega_0\tau} \quad \text{with} \quad \omega_0 = \frac{2\pi}{\Delta\tau} \tag{3.25}$$

This allows us to calculate the Fourier transform of the sampled function $f^*(\tau)$ by invoking the convolution theorem (Eqn. 3.17):

$$F^*(\omega) = \mathscr{F}(f(\tau)\text{Ш}_{\Delta\tau}(\tau)) \tag{3.26}$$

$$= \frac{1}{\Delta\tau}\sum_{n=-\infty}^{\infty} \mathscr{F}(f(\tau)) * \mathscr{F}(e^{in\omega_0\tau}) \tag{3.27}$$

$$= \frac{1}{\Delta\tau}F(\omega) * (\sum_{n=-\infty}^{\infty} \delta(\omega - n\omega_0)) \tag{3.28}$$

$$= \frac{1}{\Delta\tau}F(\omega) * \text{Ш}_{\frac{2\pi}{\Delta\tau}}(\omega) \tag{3.29}$$

$$\tag{3.30}$$

The last equation shows that the Fourier transform of a sampled function $f^*(\tau)$ results in the spectrum of the continuous function $f(\omega)$ convoluted with a Dirac-comb, i.e. the spectrum repeats itself in the frequency domain with the period $\frac{2\pi}{\Delta\tau}$ (Figure 3.10). Therefore, as long as these spectral copies do not overlap, we can uniquely identify every frequency component of the signal. This is exactly the case when the bandwidth of the signal ($2 \times \omega_{max}$[h]) is smaller than the distance between two spectral copies:

$$\Delta\tau < \frac{2\pi}{2\omega_{max}} \tag{3.31}$$

$$\Delta\tau < \frac{1}{2f_{max}} \tag{3.32}$$

The minimum sampling rate $f_{Nyq} = 1/(\Delta\tau)$ at which $\omega_{max}$ can uniquely be identified is known as the Nyquist frequency. It is important to note that the above discussion only holds for bandwidth limited signals. Otherwise, there exists a possible overlap between the replica of the spectrum. Therefore, frequencies higher than $\omega_{max}$ will be present in the observation window $[0, \omega_{max}]$. This backfolding can only be prevented by limiting the time domain signal to the expected frequency range with the help of optical and/or electronic filters.

A similar line of thought can be invoked to show that the frequency sampling $\Delta\omega$ is given by:

$$\Delta\omega = \frac{\pi}{\tau_{max}} \tag{3.33}$$

Thus, the frequency sampling $\Delta\omega$ (not the resolution) is given by the maximum retardation $L$. Lastly, representing the frequency in units of wavenumbers ($\nu = \omega/(2\pi c)$ in $\text{cm}^{-1}$), provides a convenient relation between retardation $x$ and

[h] The information content of the spectrum at negative frequencies is identical to the content at positive frequencies. Both halves of the spectrum can be interconverted as long as the time domain signal is known.

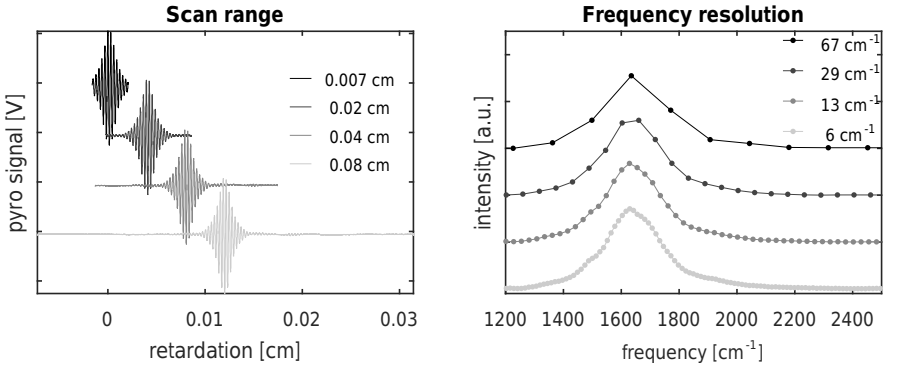


FIGURE 3.11. Interferograms with increasing scan range (left) and the corresponding spectra with increasing frequency resolution (right).

frequency sampling:

$$\Delta\nu[cm^{-1}] = \frac{1}{2x_{max}[cm]} \tag{3.34}$$

$$\nu_{max}[cm^{-1}] = \frac{1}{2\Delta x[cm]} \tag{3.35}$$

Next, we inspect the impact of scan range and sampling rate to provide some examples for the topics discussed in the previous section. Figure 3.11 shows interferograms with increasing scan range and the corresponding interferograms, and it demonstrates the inverse proportionality between maximum retardation and resolution (Eq. 3.33). Figure 3.12a shows the same interferogram sampled with different time steps and Figure 3.12b shows the corresponding spectra. Not only does this figure illustrate the effect of sampling rate on the maximal resolvable frequency, it also shows the effect of backfolding when the spectral features of interest are above the Nyquist frequency.

### 3.3.2 HARDWARE IMPLEMENTATION: MACH-ZEHNDER INTERFEROMETER

Figure 3.13 shows the design of the Mach-Zehnder interferometer, which was adapted from Ref.[78] The small footprint (15 x 15 cm) of the implementation allows for a flexible placement in the experimental setup. In the interferometer, the input beam is split into two using a 50:50 beamsplitter. The resulting beams are guided over two retroreflectors, after which they are recombined on a second beamsplitter. One of the retroreflectors is static while the other is mounted on a computer-controlled translation stage (PI, M-111.DG). The Mach-Zehnder interferometer provides two accessible output beams[i], with interference patterns that are each others opposites.

[i] in contrast to the Michelson interferometer, where one output beam is colinear with the input.

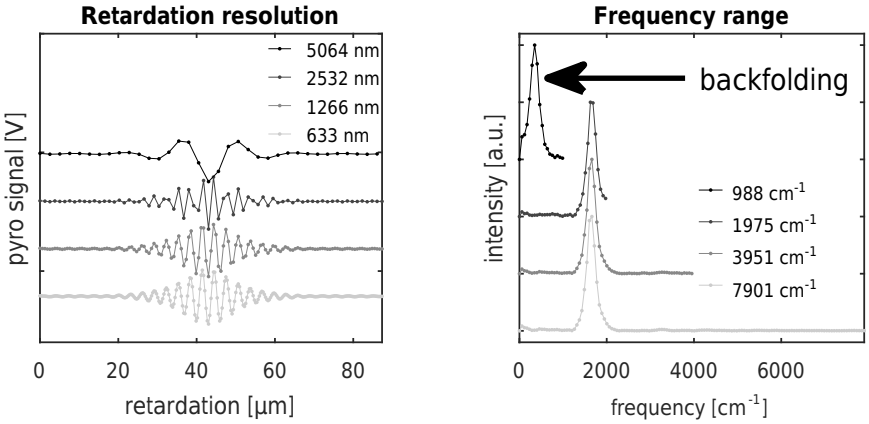


FIGURE 3.12. Interferograms with decreasing sampling step sizes (left) and the corresponding spectra with increasing maximum frequency (right). The black arrow indicates backfolding of the spectrum due to undersampling of the interferogram.

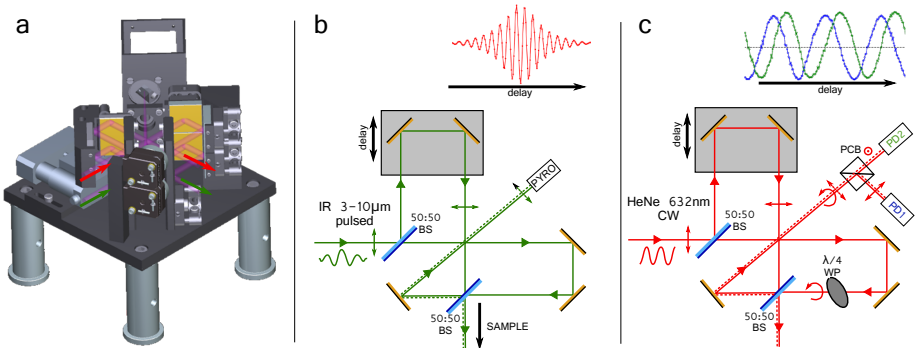


FIGURE 3.13. Mach-Zehnder interferometer geometry. a: Three-dimensional rendering of the bread board design. b: Schematic representation of the infrared beam path and interference pattern measured by the pyroelectric detector (inset, top). c: Schematic representation of the HeNe beam path and interference pattern measured by the photodiods (inset, top). Arrows indicate the polarization and the propagation direction. PD: photodiode. PCB: polarizing cube beamsplitter. WP: waveplate. BS: beam splitter.

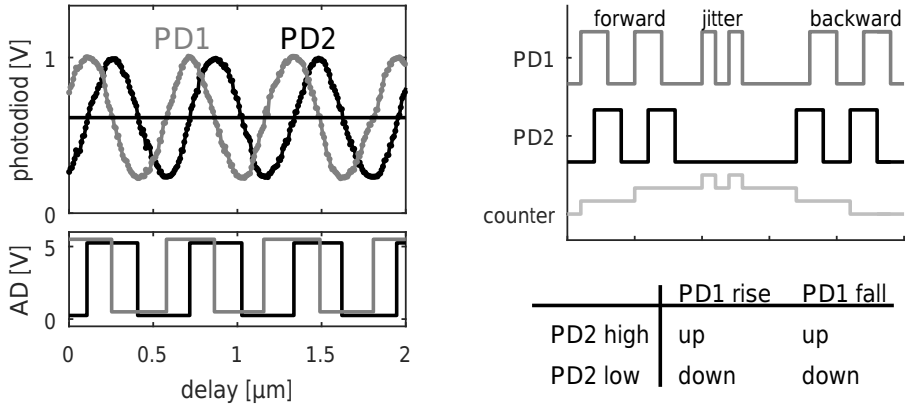


FIGURE 3.14. Delay distance sampling via counting interference fringes. Left: Raw photodiode signal (top) and corresponding digital TTL signal (bottom, offset for clarity). Right: Counting logic (bottom) and example signals for both photodiods and the corresponding counter values.

Our interferometer is, in fact, a double interferometer with two almost identical beam paths (an infrared beam path and a visible HeNe beam path) stacked on top of each other. The infrared beam path (Fig. 3.13b) serves to generate a pair of pump pulses while the HeNe beam path (Fig. 3.13b) is used to precisely determine the delay between the two infrared pulses by counting the HeNe interference fringes.

The counting of the HeNe fringes is implemented using a so-called quadrature counting scheme, as is explained in Figure 3.14. In this scheme two HeNe interferograms with a phase difference of 90° are generated (Figure 3.13). This makes it possible to distinguish between movements of the dynamic arm in the forward and backward direction. In order to create two out-of-phase HeNe interferograms a $\lambda/4$ plate is placed in one of the interferometer arms, thereby converting the linear polarization of the light to circular. The circularly polarized light from the first arm is recombined with the linearly polarized light from the second arm, after which the recombined beam is again split into two beams with the help of a polarizing cube beam splitter (oriented at 45° with respect to the linearly polarized input beam). The interference fringes in these two output beams are exactly 90° out-of-phase with respect to each other, and they are recorded using two photodiodes. The photodiode outputs are converted to binary signals using analog-to-digital converters (AMOLF) and fed into the quadrature counter integrated in the DAQ-cards. Figure 3.14 summarizes the counting procedure.
The quadrature counter method provides several advantages:

- The scanned delay is intrinsically measured on an equidistant grid (defined by the HeNe wavelength) which is necessary for the Fourier transformation of the interferogram.
- The displacement of the dynamic arm can be determined very accurately ($< \lambda_{HeNe}/2$) because the measurement is not affected by the limitations of the

translation stage, such as backlash ($\sim$2 $\mu$m ) and unidirectional repeatability (0.1 $\mu$m ).

- Using the quadrature-counting scheme the direction of the movement can be determined, which is not possible with a single-photodiode fringe counting.
- The combination of the above points allows for measurements with very fast scan rates ($>$0.3 mm/s).

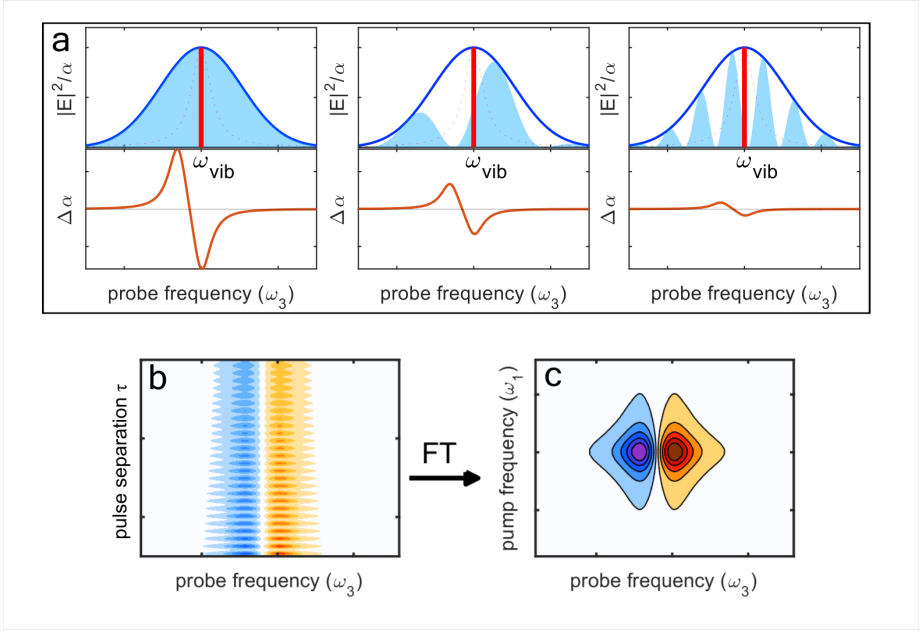


FIGURE 3.15. Generating a 2DIR spectrum.
a) Pump-probe spectra at different retardation times $\tau$. The excitation efficiency of a vibration at $\omega_{vib}$ (top, red line) and therefore the amplitude of the generated pump-probe signal (bottom) depends on the overlap of the spectral density of the pump spectrum (top, blue area) and the spectrum of the vibration. The blue line (top) shows the envelope of the pump spectrum. b) 2DIR signal as a function of pump pulse separation $\tau$ and c) as a function of pump frequency $\omega_1$.

### 3.3.3 PRINCIPLES OF FOURIER TRANSFORM 2DIR SPECTROSCOPY

To understand how a 2DIR spectrum is measured in the time-domain, we first need to understand how the Mach-Zehnder interferometer modifies the pump spectrum and, second, what influence this modified pump spectrum has on the resulting nonlinear signal.
The MZ interferometer converts the pump pulse into a pulse-pair with an adjustable time separation $\tau$. The electric field of the pump at the sample position is given by:

$$E(t,\tau)_{pump} = E_{stat}(t) + E_{dyn}(t) = E_{stat}(t) + E_{stat}(t+\tau) \tag{3.36}$$

where $E_{stat}$ and $E_{dyn}$ refer to the electric field from the dynamic ($E(t+\tau)$) and the static arm ($E(t)$) of the interferometer, respectively. The corresponding pump spectrum after the interferometer is given by:

$$I(\omega,\tau) = 2|E_{stat}(\omega)|^2(1+\cos(\omega\tau)) \tag{3.37}$$

This equation shows that the effect of the MZ interferometer is to modulate the spectrum of the original pump pulse by interference fringes. These intensity

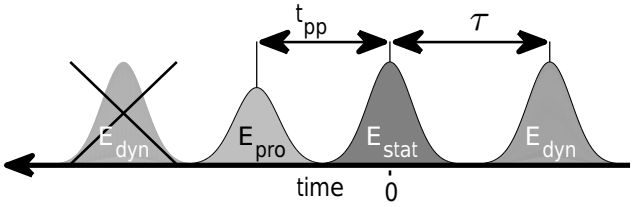


FIGURE 3.16. Pulse sequence in a 2DIR experiment.

oscillations originate from the cosine-term, and the frequency spacing between two fringes is determined by the time delay $\tau$.
In the following, we take a phenomenological approach and examine the absorption change generated by the interaction of the pump pulse pair with a molecular vibration (characterized by a resonance frequency $\omega_{vib}$) at a fixed pump-probe delay $t_{pp}$ (Fig. 3.15). The excitation efficiency of the molecular vibration, and hence the amplitude of the pump-probe signal, is given by the spectral density of the pump pulse pair at the fundamental frequency $\omega_{vib}$. This means that, if the retardation $\tau$ is scanned, the amplitude of the pump-probe signal will oscillate with a frequency $\omega_{vib}$. Recording the absorption change as a function of $\tau$ (Fig. 3.15a) results in a two-dimensional time-frequency map $\Delta\alpha(\tau, t_{pp}, \omega_3)$ (Fig. 3.15b). Fourier transformation of $\Delta\alpha(\tau, t_{pp}, \omega_3)$ along $\tau$ yields a frequency-frequency correlation plot $\Delta\alpha(\omega_1, t_{pp}, \omega_3)$, or in other words the 2DIR spectrum (Fig. 3.15c).

### 3.3.4 DATA TREATMENT

This section discusses some additional steps that need to be taken after acquiring the time-domain signal to prevent introducing artifacts and to achieve 2DIR spectra with the highest possible resolution. In a FTIR measurement one usually records a symmetric double-sided interferogram by scanning the retardation $\tau$ from $-\tau_{max}$ to $+\tau_{max}$. In 2DIR spectroscopy this approach does not work because the signal is not symmetric around $\tau = 0$ (due to the presence of the probe pulse). We solve this issue by scanning the pulse from the dynamic arm of the interferometer $E_{dyn}$ only in one direction, which is away from the probe pulse (see Figure 3.16). Hence, the time-domain signal in FT-2DIR is defined on the domain $\tau \in [0, \infty)$. Practically, a slightly larger $\tau$-range is measured during the experiment, and the data set is truncated afterwards to only contain points where $\tau \geq 0$. Unfortunately, one cannot easily find the point where $\tau = 0$ by simply inspecting the nonlinear signal. That is because there is also a nonlinear signal at negative values of $\tau$ (which can be seen as artifact in the current context). The problem is that missing the point $\tau = 0$, by even as little as one sampling point, leads to lineshape distortions in the frequency domain as is illustrated in Figure 3.17. Since the time-domain 2DIR signal represents a single-sided interferogram (i.e. $\tau \geq 0$), its Fourier transform yields complex valued lineshapes. The highest possible spectral resolution is achieved by selecting the real part of the frequency-domain signal since it provides absorptive lineshapes, which have the

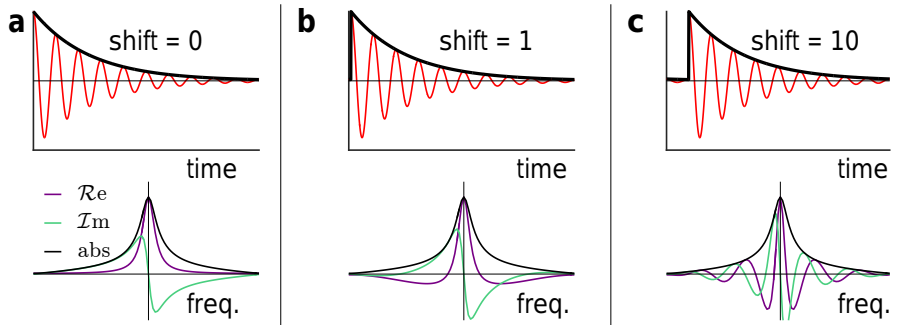


FIGURE 3.17. Single-sided exponential and its Fourier transform at a circular permutation (shift) of 0 (a), 1 (b), 10 (c) data points.

narrowest possible linewidth. Misjudging (shifting) the origin of the retardation axes by $\delta$ in the time-domain signal $A(\tau)$ introduces a linear phase $\phi_\delta$:

$$\mathcal{F}\{A(\tau+\delta)\} = \mathcal{F}\{A(\tau)\} \cdot e^{-i2\pi\delta\omega} \tag{3.38}$$

$$= A(\omega) \cdot e^{-i\phi_\delta(\omega)} \tag{3.39}$$

that mixes the real and imaginary part of the spectrum resulting in the aforementioned lineshape distortions.

The solution for this phasing problem is built into the Mach-Zehnder interferometer. One of its output beams is used to excite the sample, and the other to simultaneously record an interferogram of the pump pulse (Fig. 3.18a,b) which is totally symmetric around the point $\tau = 0$. In principle, we could find the sampling point closest to $\tau = 0$ by taking the minimum of the pump interferogram. However, it turns out that we need to determine $\tau = 0$ more precisely than one sampling point. This is achieved by the following approach. As follows from Eq. 3.39, the 2DIR signal can be completely compensated for the shift of the origin by multiplying the frequency domain signal with the correct phase function before taking the real part. The correct phase function is the function that minimizes the imaginary part of the pump spectrum. This follows from the fact that, contrary to the 2DIR response, the pump interferogram is a symmetric function of $\tau$. Figure 3.19 shows a 2DIR spectrum with and without applying the phase correction.

### ZERO PADDING

In Fourier transform spectroscopy, zero padding refers to the refinement of the frequency grid, by appending zeros to the time-domain data. In general, if the signal $I(\tau)$ has decayed completely at its last sampling point $N-1$, appending zeros does not change the informational content, but effectively increases the length of the data set. Since the frequency spacing $\Delta\omega$ after Fourier transformation is inversely proportional to the acquisition length $\tau_{max}$:

$$\Delta\omega \propto \frac{1}{\tau_{max}} \tag{3.40}$$

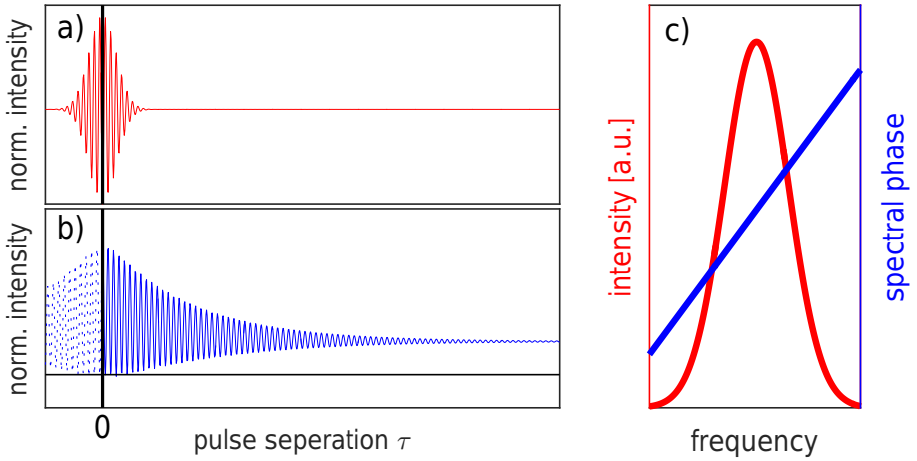


FIGURE 3.18. Phase correction of the 2DIR spectrum. Panel a) shows the interferogram of the pump acquired with the pyroelectric detector inside the Mach-Zehnder interferometer, and panel b) shows the simultaneously acquired time-domain 2DIR signal (for one frequency). Fourier transformation of the pyro signal (panel c) allows to extract the spectral phase which in turn can be used to both, remove data points in the 2DIR spectrum acquired for negative time delays ($\tau < 0$, dotted line in panel b), and to compensate for the spectral phase of the Fourier transform 2DIR time-domain data.

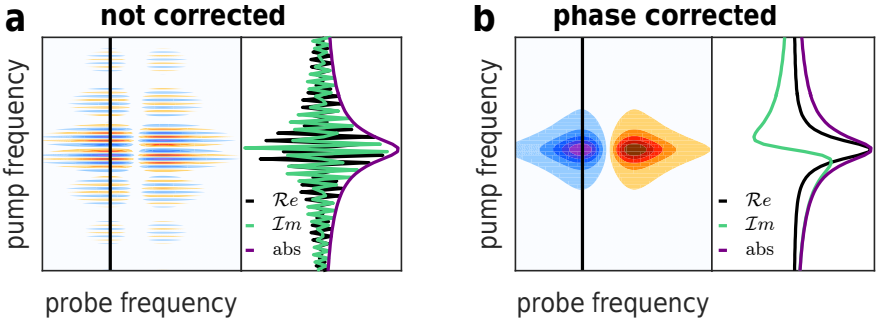


FIGURE 3.19. Effect of phase correction on the 2DIR spectrum. Panel a) shows the real part of $\Delta\alpha_{2D}(\omega_1, t_{pp}, \omega_3)$ without phase correction, and panel b) the phase corrected 2DIR spectrum. The right side of each panel shows the real and imaginary part and the absolute value for one probe frequency (black line) of the 2DIR spectrum.

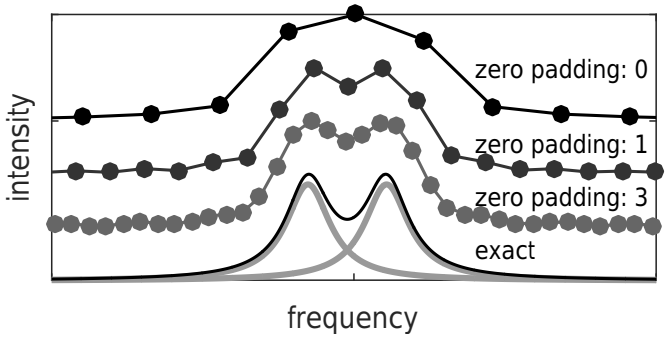


FIGURE 3.20. Zero-padding the Fourier transform of a single-sided function. A function consisting of two single-sided oscillating terms, which are close in frequency, was Fourier transformed with no zeros padded; the same amount of zeros added as used data points; and three times the amount of data points. The exact Fourier transform is shown as a comparison.

the addition of zeros at the end of the data set leads to an increase of the frequency sampling rate. This procedure, does not increase the resolution, instead it results in a trigonometric interpolation of the frequency domain data.[81]
In contrast, as is well known in NMR spectroscopy, the situation is different for a single-sided time-domain function. In this case one can actually achieve a resolution enhancement of at most a factor of two in the spectrum by zero padding the time-domain data. As was shown in ref.[84] this can intuitively be understood by the fact that zero padding (by a factor of two) effectively adds the information content of the imaginary part of the spectrum to the real part of the spectrum (which is the part we usually inspect). Further zero padding only results in an additional interpolation of the spectrum. Figure 3.20 demonstrates that zero padding a single-sided function which contains two oscillating terms which are close in period can can result in a distinction of the two peaks in the frequency domain.

### 3.3.5 CHOPPER STATE AND INTERFEROMETER SPEED

In the previous sections, the measurement of a 2DIR time-frequency map $\Delta\alpha(\tau, t_{pp}, \omega_3)$ was described as an acquisition of a pump-probe spectrum for every pump pulse separation $\tau$. To this end, one needs to perform a transmission measurement for at least two laser shots per retardation step: one in the presence ($T$) and one in the absence ($T_0$) of the pump pulse. Although this is a valid approach, it is not strictly necessary in time-domain 2DIR because the modulation as a function of $\tau$ allows us to extract $\Delta\alpha_{2D}$ via the Fourier transform. Therefore, it is possible to skip the measurement of $T_0$ (the not-pumped spectrum) which results in a reduction in measurement time of a factor of 2 for the same signal-to-noise ratio. Figure 3.21 demonstrates this by comparing two 2DIR measurements, performed under the same conditions, with and without the usage of a chopper. The figure also shows that the noise in the measurements without chopper is almost independent of the speed of

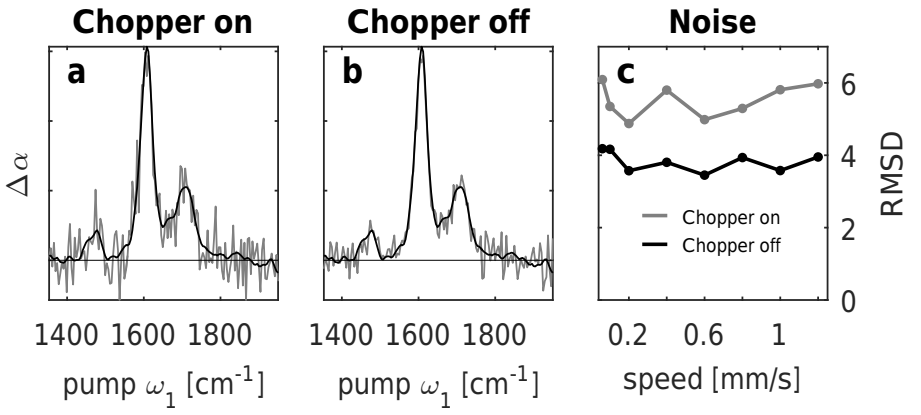


FIGURE 3.21. 2DIR acquisition with and without Chopper. Panel a) and b) show 2DIR measurements for one probe frequency which were performed under the same conditions (stage speed: 0.6 mm/s) except for the state of the chopper. To estimate the relative noise, the root mean square deviation to a high signal-to-noise measurement (black) was calculated. c) compares these values for different speeds of the interferometer translation stage.

the translation stage, and $\sim\sqrt{2}$ lower when compared to measurements with chopper. The most straightforward way to acquire the full time-domain spectrum $\Delta\alpha(\tau, t_{pp}, \omega_3)$ is to move the translation stage one time step $\Delta\tau$ at a time. But, in reality, the control mechanics of the stage make this option undesirable, since every movement to a specific target position is accompanied by considerable overhead time (∼0.1–0.5 s) and inaccuracy. We circumvent both problems, by continuously moving the stage between the two end points which define the intended range; and by reading out the counter given by the HeNe interference fringes (instead of reading the position from the stage controller).

It turns out that the speed of the translation stage has a noticeable effect on the spectrum of the noise. Figure 3.22 compares two measurements under the same conditions but at different speeds of the interferometer translation stage. Pronounced fluctuations of the signal are present in the measurement at slow speeds (0.06 mm/s) but are lacking at fast speeds (0.6 mm/s). Since at a speed of 0.6 mm/s only every 2nd to 3rd time point is sampled in one pass, multiple scans of the same range are needed to fill every grid point. This effectively scrambles the noise correlations (low frequency) between different time points and redistributes the spectral density of the noise more equally throughout the spectrum, reducing spectral features which might be interpreted as real nonlinear signals.

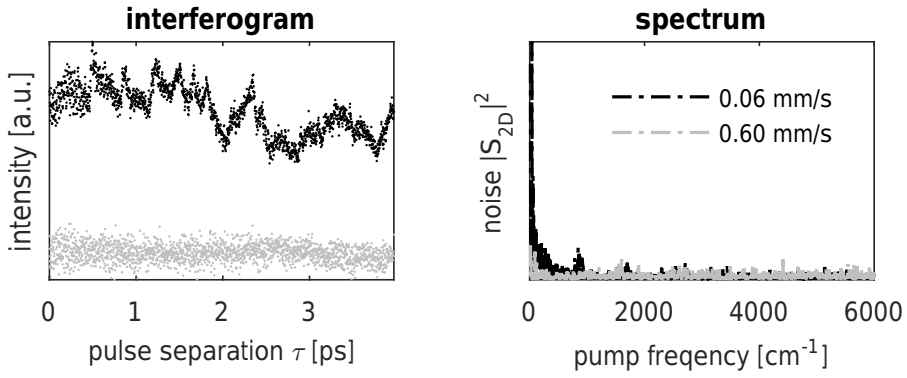


FIGURE 3.22. Dependence of the noise in 2DIR on the speed of the interferometer translation stage a) 2DIR interferogram for one probe frequency at two different interferometer scanning speeds and b) corresponding energy spectral density.

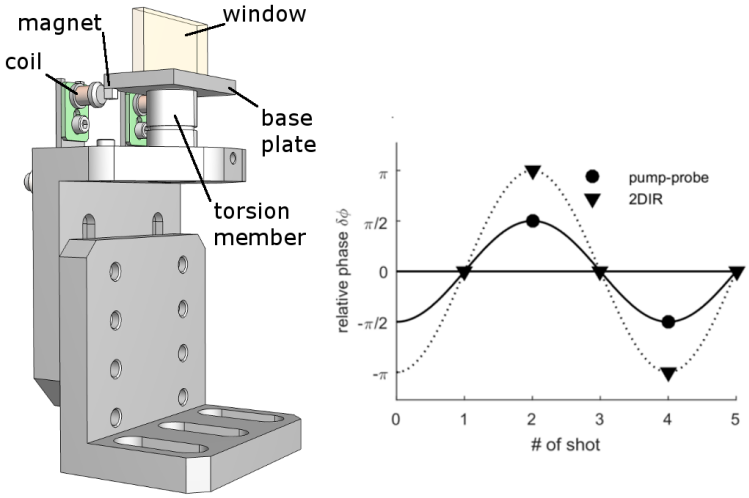


FIGURE 3.23. left: CAD model of the wobbler. right: Possible schemes for scattering suppression in pump-probe and 2DIR experiments.

## 3.4 SCATTERING SUPPRESSION

### 3.4.1 PRINCIPLE

Scattering poses a severe problem, both in pump-probe and 2DIR spectroscopy, since it can lead to strong artifacts which obscure the transient signal. It occurs when a small fraction of the pump light reaches the detector where it interferes with the probe light. There exist many possible sources for stray light, like scratches or contamination (dust, fingerprints) on the optics used, and most crucially the sample windows. Sometimes the sample itself can lead to strong stray light, examples encountered in this thesis are protein aggregates (Chapter 4) and metallic nanostructures (Chapter 5). If we assume that only a small fraction $\alpha \ll 1$ (e.g. 0.001) of a strong pump pulse $E_{pump} \approx 100 \times E_{probe}$ reaches the detector, then the measured total intensity is given by:

$$|E_{probe} + \alpha E_{pump}|^2 \tag{3.41}$$

$$= |E_{probe}|^2 + \alpha^2 |E_{pump}|^2 + 2\alpha \mathcal{R}e(E_{probe} E^*_{pump}). \tag{3.42}$$

The last term in Eq. (3.42) introduces an interference term between the pump and probe field. This interference term can have a similar or even greater amplitude than the absorption change originating from molecular vibrations, and, for convenience, we will refer to it as scattering for the rest of the chapter.
For simplicity, we are going to assume that the electric fields in the frequency domain are bandwidth limited and can be described by:

$$E(\omega) = A(\omega) e^{-i(\omega t + \phi)} \tag{3.43}$$

with the real-valued envelope $A(\omega)$, and the phase factor $\phi$. Since the scattering signal is an interference between the pump and the probe field its spectral shape strongly depends on the time separation $\Delta t = t_{pp}$ between the two fields:

$$\mathcal{R}e(E_{probe} E^*_{pump}) = |A(\omega)_{pump}||A(\omega)_{probe}| \underbrace{|\cos(\omega \Delta t + \delta\phi)}_{S(\delta\phi)} \tag{3.44}$$

where $\delta\phi$ is the relative phase between pump and probe. From Eq. (3.44) we see that with increasing delay $\Delta t$ the separation between adjacent interference fringes becomes smaller, but the amplitude of S does not change. Thus, the scattering signal becomes increasingly larger, compared to the pump-probe signal which decays with the vibrational lifetime. The phase term $\delta\phi$ has no influence on the periodicity or the amplitude of S, but leads to a shift along the frequency axes.
In most experiments, we perform multiple measurements for every time delay $\Delta t = t_{pp}$, e.g. in pump-probe experiments one usually acquires 1000 shots per delay. Hence, if we find a way to modify the relative phase, therefore shift the scattering along the frequency axes, on a shot-to-shot basis, it is possible to find conditions where the average scattering signal cancels out. To give one example, the average

scattering signal vanishes if two consecutive measurement have a relative phase of $\pi$:

$$\frac{1}{2}\left(S(-\frac{\pi}{2})+S(\frac{\pi}{2})\right)=\frac{1}{2}\left(\cos\left(\omega\Delta t-\frac{\pi}{2}\right)+\cos\left(\omega\Delta t+\frac{\pi}{2}\right)\right) \tag{3.45}$$

$$=\frac{1}{2}\left(\cos(\omega\Delta t)\cos\left(\frac{\pi}{2}\right)\right)=0 \tag{3.46}$$

This can be generalized for any integer valued subdivision $n$ of one period ($2\pi$) of the phase:

$$\sum_{k=1}^{n}S(\frac{2\pi}{n}k+c)=\sum_{k=1}^{n}\cos\left(\omega\Delta t+\frac{2\pi}{n}\cdot k+c\right)=0 \quad n=2,3,4,... \quad c\in\mathbb{R} \tag{3.47}$$

Thus, there are infinitely many possibilities to adjust the phase between consecutive measurements for which the scattering signal vanishes in the average.
In practice there are two common approaches to modulate the relative phase between the pump and probe pulse: one can either directly modify the phase of either pump or probe by employing a pulse shaper, or one can introduce a small additional delay $\Delta t+\frac{\delta\phi}{\omega_0}$ which results in quasi-phase shift. We will focus on the second approach.
Although significantly simpler than the pulse shaper approach, the introduction of some additional path length has the downside of only yielding the desired phase $\delta\phi$ for one specific frequency $\omega_0$. We can consider the implications by modifying Eq. (3.46):

$$\cos(\omega\Delta t)\cos\left(\frac{\pi}{2}\frac{\omega}{\omega_0}\right)=0 \tag{3.48}$$

The $\cos\left(\frac{\pi}{2}\frac{\omega}{\omega_0}\right)$-term shows that perfect scattering suppression can only be achieved at the frequency $\omega_0$, and that the cancellation becomes less effective for increasing frequency deviation from $\omega_0$.

### 3.4.2 HARDWARE IMPLEMENTATION: WOBBLER

During all experiments in this thesis the relative phase was adjusted with the help of a ZnSe-window which was inserted into the pump beam path. The length of the optical path was then modulated by changing the angle of incidence. The window is mounted on top of a torsion oscillator, where a flexure bearing is used as a spring, and displacement is achieved by modulating the voltage through a coil (electromagnet) which interacts with a magnet attached to the base plate. The oscillating voltage is synchronized to the laser trigger, and the relative phase can be adjusted by changing the amplitude of the voltage and by introducing a delay to the laser trigger. Figure 3.23 shows the design of the so-called wobbler.
Next, let us consider a possible implementation for pump-probe spectroscopy. Since the laser system used in our experiments operates at 1 kHz, the fastest possible modulation with two alternating relative phase values ($\delta\phi=\pi$) is 250 Hz, since every other shot is chopped and does not contribute to the scattering suppression. Figure

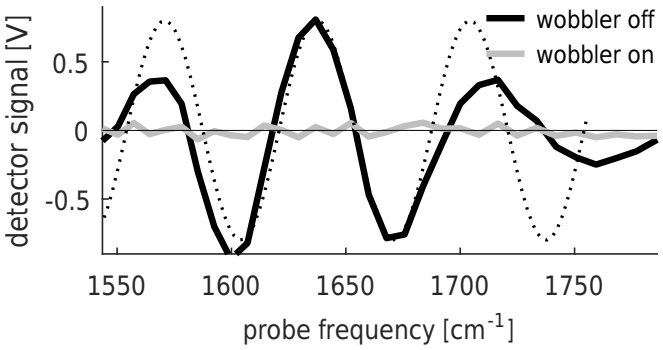


FIGURE 3.24. Example of scattering suppression with the wobbler using the pump-probe scheme. Shown are the background (probe on, pump off) subtracted probe signals at a center frequency of 1660 $cm^{-1}$ and a pump-probe delay $\Delta t = 0.5$ ps. The black dotted line indicates the expected scattering signal according to Eq. (3.44).

3.23 shows one possible modulation scheme where consecutive shots (including not pumped ones) have the relative phase: 0, $\pi/2$, 0, $-\pi/2$. Figure 3.24 shows a pump-probe measurement in a highly scattering sample with and without employing the wobbler.

During 2DIR experiments the chopper is not used (see Sec. 3.3.5 ), rendering the previously introduced modulation scheme less efficient because the average scattering signal does not fully vanish. Since the frequency of the wobbler is fixed to 250 Hz, it would be convenient to have an alternative modulation scheme for 2DIR spectroscopy which still operates at the same driving frequency. Figure 3.23 shows how this can be achieved using relative phases of 0, $\pi$, 0, $-\pi$ for 4 consecutive measurements[j].

The choice of the window material will impact by how far one has to tilt the window to achieve a certain relative phase. To introduce a change in phase of $\delta\phi$, the optical beam path has to be extended by:

$$\delta\phi(\Delta l) = \frac{\Delta l\, \omega n(\omega)}{c} \tag{3.49}$$

where c is the speed of light and $n(\omega)$ the refractive index of the medium. Figure 3.25 depicts a schematic representation of the light path through the wobbler window of thickness $d$ and refractive index $n$. Increasing the angle of incidence (tilting the window) from $\alpha$ to $\alpha + \Delta\alpha$, extends the optical path length by:

$$\Delta l(\alpha, \Delta\alpha) = \Delta s + \Delta t - \Delta u \tag{3.50}$$

where $\Delta s$ is the change in optical path length inside the window, $\Delta u$ the reduction of the path length after the window and $\Delta t$ the additional path due to the displacement

[j] Using the two introduced schemes has the additional advantage that when switching from pump-probe to 2DIR experiments one just has to double the amplitude of the used voltage.

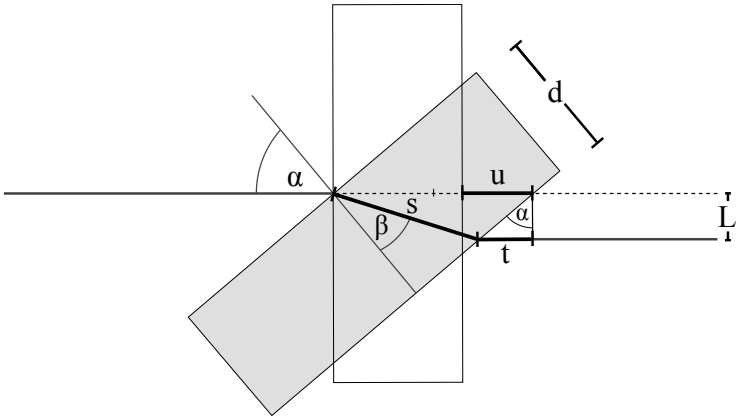


FIGURE 3.25. Schematic representation of light path through the wobbler window (top view)

of the beam after the window[k]. Employing Snell's law[l], it is straightforward to find an expression for the path lengths $s$, $t$ and $u$:

$$s = \frac{d}{\cos(\beta(\alpha))} \tag{3.51}$$

$$u = d\left(1 - \frac{1}{\cos(\alpha)}\right) \tag{3.52}$$

$$\begin{aligned} t &= L\tan(\alpha) \\ &= d\frac{\sin^2(\alpha)}{\cos(\alpha)}\left(1 - \frac{1}{n}\frac{\cos(\alpha)}{\cos(\beta(\alpha))}\right) \end{aligned} \tag{3.53}$$

Substituting the angle differentials of the last three equations into Eq. (3.50) allows us to determine the change in path length $\Delta l$ for a given angle change $\Delta\alpha$ as a function of angle of incidence $\alpha$. In general, it is favorable to operate the wobbler at Brewster's angle, to minimize losses due to reflection. Figure 3.26a shows that the path-length change inside the window $\Delta s$ is always positive, whereas the sign of the path length change outside of the window $\Delta t - \Delta u$ depends on the refractive index. Still, the total length change $\Delta L$ as a function of angle of incidence is monotonically increasing, independently of the window material (Fig 3.26b).

[k]This is justified since at the end of the beam path we use a parabolic mirror to focus into the sample, and parallel translation of the light source does not change the path length to the focal point of parabolic mirrors (Fermat's principle).[85]

[l]For the current discussion we are going to assume $n_{air} = 1$ resulting in $\sin(\alpha) = n\sin(\beta)$ for Snell's law.

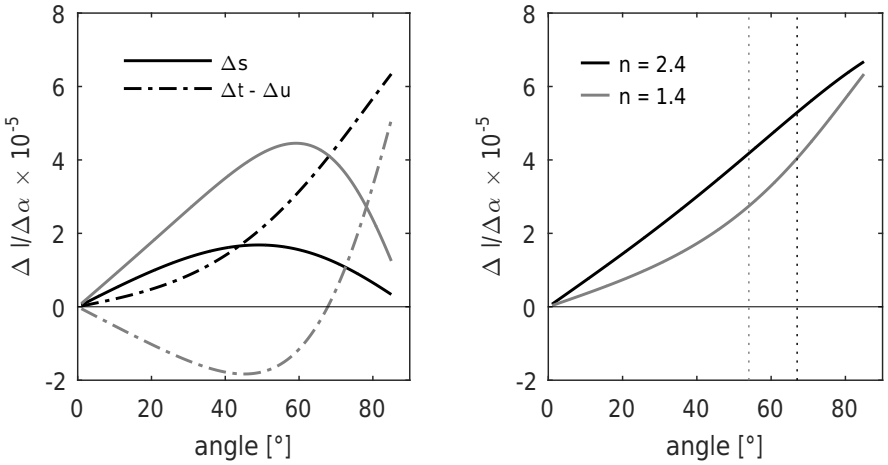


FIGURE 3.26. Change in optical path length upon changing the angle as a function of angle of incidence for a 4 mm window. a) The straight lines show the increase of optical path length inside the windows $\Delta s$, the dot-dashed lines show the increase in optical path length after the window $\Delta t - \Delta u$. b) Total optical path length difference $\Delta l/\Delta\alpha$. The dotted lines mark the Brewster's angle. The curves were calculated for ZnSe (n=2.4 at 6 μm) and $CaF_2$ (n=1.4 at 6 μm).

## 3.5 NANO FABRICATION

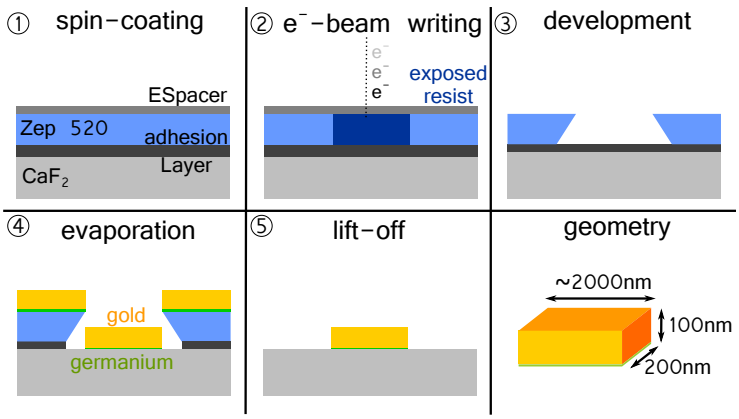


FIGURE 3.27. Electron beam lithography: fabrication process.

In Chapter 5 we will investigate how the signals in nonlinear infrared spectroscopy can be enhanced with plasmonic nanostructures. These gold nanoantennas were fabricated on $CaF_2$-substrates by electron beam lithography. Figure 3.27 outlines the fabrication process. In the following description we will focus on the objective of every fabrication step. Details about the specific parameters for every step are given

in the corresponding tables.

0. Before the actual fabrication process is started, the substrates are thougtoughly cleaned. To this end, the substrates are first rinsed with isopropanol and subsequently exposed to an $O_2$ plasma (Plasmalab 80+, strike pressure: 30 mbar) for 20 sec.

1. In the first step, the sample is prepared for the exposure with electrons. The main ingredient is the positive resist (ZEON, ZEP520A) which, when exposed to the electron beam, will change its molecular structure allowing for a selective removal later on. To improve the adhesion between the substrate and the resist an initial layer of hexamethyldisilazane (HDMS, <1 nm) is applied. In the next coating step the actual resist is added. Since an insulating substrate is used, a conductive polymer (∼20 nm, ESpacer 300Z) is needed in the last coating step to prevent charge accumulation during the writing process. All materials are applied by spincoating (Karl Suss Delta 80) which allows for precise control of the layer thickness down to several nanometers.

| Material | Function | Spincoating | | | Baking | |
|---|---|---|---|---|---|---|
| | | Accel. [rpm/s] | Speed [rpm] | Time [s] | Temp. [°C] | Time [min] |
| HDMS | Adhesion | 4000 | 1000 | 50 | 150 | 1 |
| Zep520A | Resist | 2400 | 1000 | 35 | 180 | 5 |
| ESpacer | Conduction | 3000 | 600 | 50 | 110 | 5 |

2. The actual nano-structuring is accomplished with the help of a scanning electron microscope (Raith, eLine) where electrons are used to write an earlier designed pattern into the resist.

| Parameter | Value |
|---|---|
| High tension [kV] | 20 |
| Aperture size [μm] | 30 |
| Typical current value [nA] | 0.3–0.4 |
| Writefield size [μm] | 200 or 400 |
| Nominal area does [μC $cm^2$] | 85 |
| Area step size [nm] | 10 |
| Calculated beam speed [mm $s^{-1}$] | 35<v<45 |
| Calculated dwell time [μs] | 0.2 <t<0.3 |

3. Next, the sample is exposed to a chemical agent (n-amyl acetate) which selectively targets and dissolves the exposed resist. This creates a mask, where the resist is removed down to the substrate at the position of the future nano structures. A slight "over-exposure" leads to tilted side walls (undercut), which is desirable for the success of the following steps.

| Step | Solvent | Function | Time [s] |
|---|---|---|---|
| 1 | $H_2O$ | Cleaning | 30 |
| 2 | $H_2O$ | Cleaning | 15 |
| 3 | NP | Start development | 105 |
| 4 | MIBK:IPA (9:1) | End development | 15 |
| 5 | IPA | Remove residual MIBK | 15 |

TABLE I. NP: n-amyl acetate, MIBK: methyl isobutyl ketone, IPA: isopropanyl alcohol

4. Afterwards, the sample is transferred into a high vacuum chamber (Nanoontje, AMOLF). The final structures are formed by thermal evaporation of an initial layer of germanium (1-2 nm) or chrome (1-2 nm), to increase adhesion between the substrate and the gold, and the consecutive evaporation of gold (100 nm). The metal source is located at a large distance ($\sim$1 m) from the substrate to ensure that the (metal) particle-stream reaching the substrate propagates parallel to the surface normal.

| Material | Current [A] | Nom. rate [nm $s^{-1}$] | thickness [nm] |
|---|---|---|---|
| Cr | 310 | 0.01 | 1-3 |
| or Ge | 215 | 0.01 | 1-3 |
| Au | 210 | 0.5 | 100 |

5. The large distance to the evaporation source, in combination with the undercut, prevents the growth of a continuous gold film, and allows to remove the resist and the unwanted residual metal layers by chemical etching. To this end, the sample is submerged in N-Methyl-pyrrolidone, which dissolves the resist and leaves the free standing gold nanostructures.

The outline procedure allows for a simultaneous structuring of 6 substrates (limited by the eLine). A variety of fields with different antenna geometries, configurations and densities can be written on every substrate. For spectroscopic purposes it has proven convenient to have a field geometry of >400x400 $\mu$m allowing for up to 60 fields per substrate.